Research Square

Preprints are preliminary reports that have not undergone peer review.
They should not be considered conclusive, used to inform clinical practice,
or referenced by the media as validated information.

High-efficiency silicon LED with ultra-wideband emission from visible to infrared at room temperature

Jiajing He

jiajinghe@siom.ac.cn

Shanghai Institute of optics and fine mechanics, Chinese academy of science https://orcid.org/0000-0002-6477-1061

Xiaobo Li

Shanghai Institute of optics and fine mechanics, Chinese academy of science

Xinyu Zhang

Global Institute of Future Technology, Shanghai Jiao Tong University

Xiaomei li

In Situ Devices Center, School of Integrated Circuits, East China Normal University

Hua Bao

Shanghai Jiao Tong University https://orcid.org/0000-0002-3524-2056

Xin Wu

In Situ Devices Center, School of Integrated Circuits, East China Normal University

Yaping Dan

Shanghai Jiao Tong University https://orcid.org/0000-0002-2983-7213

Jun Wang

Shanghai Institute of Optics and Fine Mechanics, Chinese Academy of Sciences https://orcid.org/0000-0003-0064-3551

Article

Keywords:

Posted Date: November 23rd, 2026

DOI: https://doi.org/10.21203/rs.3.rs-11641697/v1

License: This work is licensed under a Creative Commons Attribution 4.0 International License.
Read Full License

Additional Declarations: There is no conflict of interest

High-efficiency silicon LED with ultra-wideband emission from visible to infrared at room temperature

Xiaobo Li[1,2]†, Jiajing He[1,2]*†, Xinyu Zhang[4], Xiaomei Li[5], Hua Bao[4], Xin Wu[5], Yaping Dan[3], Jun Wang[1,2]

[1]Department of Interdisciplinary Photonics, Shanghai Institute of Optics and Fine Mechanics, Chinese Academy of Sciences, Shanghai 201800, China.
[2]Center of Materials Science and Optoelectronics Engineering, University of Chinese Academy of Sciences, Beijing 100049, China
[3]Global College, Shanghai Jiao Tong University, Shanghai 200240, China
[4]Global Institute of Future Technology, Shanghai Jiao Tong University, Shanghai 200240, China
[5]In Situ Devices Center, School of Integrated Circuits, East China Normal University, Shanghai 200241, China.

*Corresponding author. Email: jiajinghe@siom.ac.cn

†These authors contributed equally to this work.

Abstract

Efficient, electrically driven light emission from silicon remains an obstacle to the monolithic integration of light sources in silicon photonic circuits, particularly at telecommunication wavelengths. Here, we report broadband photoluminescence and electroluminescence from a standard 220-nm silicon-on-insulator platform modified by femtosecond-laser treatment. The treated silicon emits across 600-1650 nm at room temperature, with a photoluminescence external quantum efficiency of ~0.3% over 900-1650 nm. A lateral PIN LED fabricated from the treated silicon operates under forward bias and delivers an output power of 28 μW at an injection current of 11.4 mA. Over the same near-infrared spectral range, the device exhibits an external quantum efficiency exceeding 0.26% and an optical power density above 20 W/cm^2. Electron microscopy reveals a periodic lattice near the Si/SiO_2 interface with an enhanced local oxygen signal. First-principles calculations and transient-absorption measurements further indicate that laser-associated oxygen incorporation substantially modifies the electronic structure and carrier dynamics of crystalline silicon. Compared with reported silicon-based LEDs, the device combines broader spectral coverage with a high optical power density while maintaining an external quantum efficiency of the same order as the best-performing devices. These results provide a route towards compact broadband silicon light sources for integrated spectroscopy, sensing, imaging and communications.

Silicon photonics provides a scalable platform for the miniaturization and high-volume manufacturing of optical systems, benefiting from its compatibility with mature semiconductor fabrication technologies. However, silicon photonic systems still rely on externally integrated light sources, which increase packaging complexity, footprint and cost[1]. As technology develops towards high integration and miniaturization, the demand for on-chip electrically-pumped light sources becomes more urgent, and the limitations of silicon in this regard need to be urgently addressed. However, as an indirect bandgap semiconductor, the light emission process of silicon involves a complex non-radiative transition. Electrons interact with lattice vibrations to satisfy momentum conservation requirements besides transition between energy states, which will greatly increase energy loss, thus seriously restricting the light-emitting efficiency of silicon[2]. In the search for solutions, incremental advances have been made through techniques such as wafer bonding, III-V semiconductor growth and the integration of gain media into silicon-compatible photonic platforms, which offer high output power and meet communication wavelengths, thereby revitalizing hope for silicon photonics[3-7]. Nevertheless, these approaches introduce additional materials, fabrication steps and thermal-budget constraints, which can complicate integration with standard complementary metal–oxide–semiconductor (CMOS) process flows and increase manufacturing costs. CMOS-compatible silicon light-emitting diodes (LEDs) have also been widely investigated, including forward-biased junction devices and reverse-biased P–I–N diodes based on impact ionization or avalanche processes[8-13]. However, their broader adoption has been restricted by low electro-optical conversion efficiencies, limited optical power densities and, in many cases, emission spectra that do not adequately cover the principal telecommunication bands. An electrically driven silicon emitter that simultaneously provides high efficiency, high power density and broad spectral coverage therefore remains highly desirable.

The need for integrated light sources extends beyond optical communications. Broadband emitters are central to applications such as Fourier-transform spectroscopy, waveguide absorption spectroscopy, micro-resonator-based sensing, optical coherence tomography and hyperspectral imaging[9,14-16]. Although some refractive-index sensors can operate with fixed-wavelength lasers, spectroscopic identification of molecules and materials generally benefits from a source that covers a wide wavelength range. Supercontinuum generation has been demonstrated experimentally in both silicon nitride and silicon waveguides, providing exceptionally broad optical bandwidths[17,18].

However, these systems typically rely on bulky, costly, and energy-intensive external continuous-wave or pulsed pump lasers that require high optical powers or peak intensities, thereby offsetting the advantages of integrated nonlinear waveguides[19,20]. Moreover, the absence of a compact, electrically driven broadband source complicates the realization of fully integrated and portable spectroscopic systems. These constraints are particularly important for wearable devices, mobile platforms and distributed sensors, for which size, electrical power consumption and system complexity must all be minimized. Developing an efficient, electrically driven broadband source directly on silicon would therefore address both a fundamental materials challenge and a practical need in integrated photonics. Achieving this goal requires strategies that modify the radiative recombination pathways and electronic structure of silicon without abandoning the standard silicon-on-insulator platform.

Here, we engineer the near-interface region of a standard 220-nm silicon-on-insulator platform using femtosecond laser treating (FLT) technology, enabling room-temperature photoluminescence and electroluminescence across 600-1650 nm. Structural characterization and first-principles calculations associate the enhanced emission with laser-induced lattice modification and oxygen incorporation near the Si/SiO_2 interface. A lateral PIN diode fabricated from the treated silicon delivers an optical output power of 28 μW at 11.4 mA, corresponding to a power density exceeding 20 W/cm^2—several orders of magnitude higher than that of other silicon-based LEDs. It also achieves an external quantum efficiency (EQE) of over 0.26% across the 900-1650 nm wavelength range. These results establish femtosecond-laser-engineered silicon as a compact, electrically driven broadband light source that can be integrated with silicon photonic circuits for spectroscopy, sensing and communications[21,22].

Results

Samples were prepared by FLT, with detailed procedures provided in the FLT section of the Methods. We measure the power-dependent photoluminescence (PL) spectra of silicon after FLT at room temperature (Fig. 1a) with an ultra-wideband luminescence in the range of 900-1650 nm. The fluorescence intensity significantly increases with rising excitation power. A direct comparison with untreated crystalline silicon shows that the FLT-treated sample exhibits a substantially stronger PL response under the reported measurement conditions (Extended Data Fig. 1), demonstrating that the

enhanced emission is associated with the laser treatment rather than the intrinsic emission of the untreated Si substrate. Complementary measurements in the visible spectral range further reveal detectable power-dependent emission below the near-infrared measurement window (Extended Data Fig. 2a), indicating that the optical response of FLT-treated silicon is not restricted to 900–1,650 nm. To quantify the excitation-power dependence, the spectrally integrated PL intensity was fitted using the power-law relation $I_{PL} \propto P^k$, where P is the excitation power, k is the power-law exponent (Fig. 1b). Two excitation regimes are identified, with fitted power-law exponents of 5.40 and 9.62, both significantly greater than 1 and exceeding those reported for materials such as silicon[23,24], InP[25] and SiGe[26]. These strongly super-linear dependences indicate that, even at room temperature, the sample exhibits ultra-high internal quantum efficiency, with minimal effects from non-radiative recombination processes such as Auger or temperature-dependent processes[27]. Consistent with the integrated PL data, the inset of Fig. 1b shows a nonlinear increase in the emitted optical power with increasing excitation power over the measured range. No clear threshold or saturation behavior is resolved from these data. The spectrally integrated visible PL also exhibits a nonlinear excitation-power dependence (Extended Data Fig. 2b), showing that excitation-density-dependent emission is observed beyond the near-infrared detection window.

Fig. 1c shows the EQE of the FLT-treated silicon, integrated over 900–1,650 nm, as a function of excitation power. The wavelength-dependent detection response was calibrated using a commercial Hamamatsu L12509-0155G LED as a reference source[28]. The EQE increases nonlinearly with excitation power and reaches a maximum measured value of approximately 0.3%. Under the reported measurement conditions, this value is approximately four orders of magnitude higher than the literature value reported for pristine silicon (10^{-7}) and approaches values reported for direct-band-gap SiGe alloys[23,26]. It is important to note that the current EQE is far from saturation (the slope has not diminished), indicating that there is potential for further increases of EQE with additional increases in excitation power. Furthermore, we have only calculated the EQE in the 900 to 1650 nm range, considering its strong emission capability in the visible range, the EQE over the entire spectrum will be greater than 0.3% (see Extended Data Fig.2). Fig. 1d displays the fluorescence lifetime of the samples before and after FLT at room temperature. The decay curves were fitted using a biexponential function, yielding time constants of τ_1=220 ps and τ_2=1883 ps for the FLT-treated sample, compared with τ_1=72 ps and τ_2=539 ps for the untreated reference. The longer decay components after FLT demonstrate that the

treatment produces a more persistent photoexcited population.

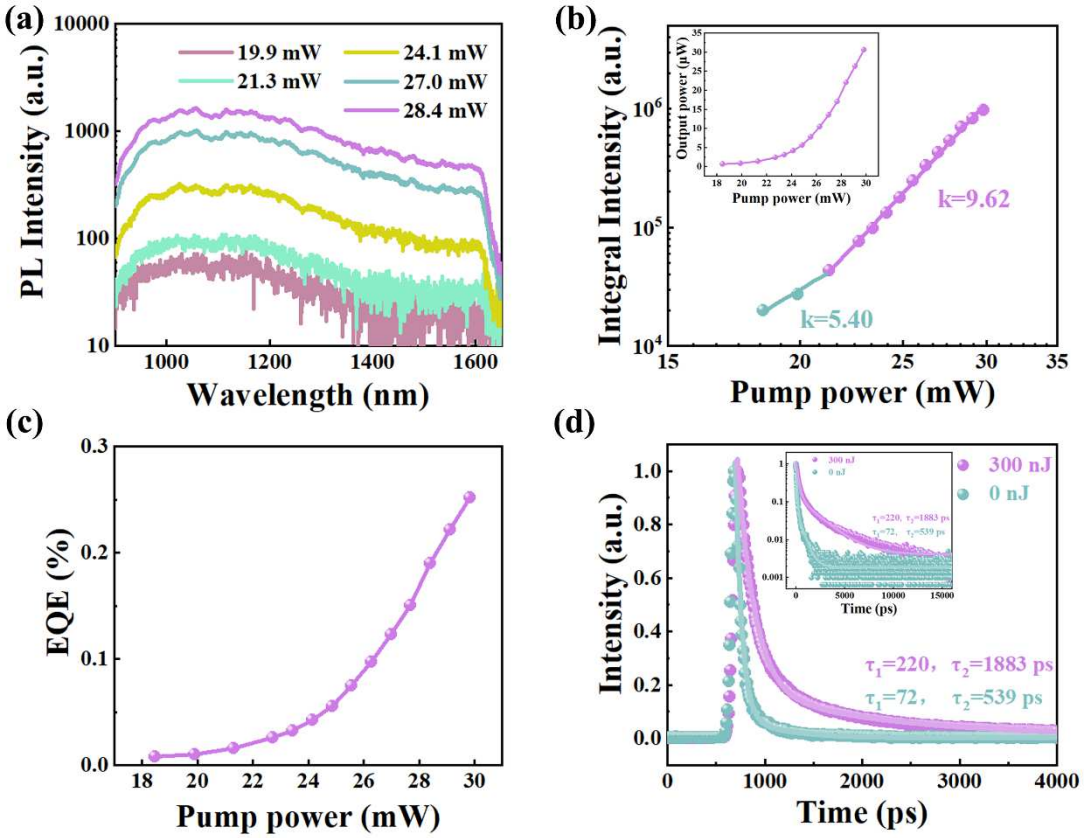

Fig. 1 | PL test of the sample. a, Excitation-power-dependent PL spectra of FLT-treated silicon. **b,** Integrated infrared PL intensity as a function of excitation power, with the straight line representing the linear fit of PL integral intensity with variable pump power (log-log scale), along with an illustration of the output power versus injection current. The illustration of the correlation between output power and pump power is included. **c,** EQE of infrared light at varying pump power. **d,** Fluorescence lifetime of silicon after FLT (532nm excitation).

Microstructural characterization of the laser-treated samples was performed using aberration-corrected transmission and scanning transmission electron microscopy (TEM). As shown in Fig. 2a, the sample exhibits a $Si/SiO_2/Si$ layered structure, with the two Si/SiO_2 interfaces marked by white dashed lines. The laser-treated regions exhibit laser-ablated holes and irregular amorphous structures. Selected-area electron diffraction (SAED) analysis revealed that laser treatment induced the appearance of super-diffraction spots in the crystalline Si—particularly at the Si/SiO_2 interface—as indicated by the white arrows in Fig. 2b. These additional reflections suggest the presence of a periodic structural modulation in the interfacial Si. As a control, the FLT sample prepared without oxygen treatment exhibited a direct transition from crystalline to amorphous Si, without an identifiable intermediate periodic defect structure or corresponding additional diffraction spots (Extended Data Fig.3).Atomic-resolution annular bright-field scanning transmission electron

microscopy (ABF-STEM) imaging revealed local structural contrast near the Si/SiO_2 interface that differs from that of the undisturbed Si lattice, suggesting local lattice reconstruction or defect formation (Fig. 2d). Atomic-resolution high-angle annular dark-field scanning transmission electron microscopy (HAADF-STEM) imaging of the region marked by the yellow box in Fig. 2d revealed a periodic lattice modulation within the Si, with a repeat distance of approximately 0.95 nm (Fig. 2e). Local FFT and SAED analyses further showed that additional reflections were observed in the region containing the periodic lattice modulation but were absent from the reference crystalline Si region (Extended Data Fig.4), supporting the assignment of the additional diffraction spots in Fig. 2b to the periodic lattice modulation. This periodic structure may account for the additional diffraction spots observed in Fig. 2b. To elucidate laser-induced changes in the local chemical environment, electron energy-loss spectroscopy (EELS) was performed on both sides of the Si/SiO_2 interface. Fig. 2c and 2f show the O-K-edge spectra acquired from the SiO_2 and Si sides of interfaces with and without the laser-induced periodic defect structure, respectively. As shown in Fig. 2f, the O-K-edge signal intensity in the defective Si region ($O_{Si\text{-}def}$) was higher than that in the reference crystalline Si region (O_{Si}), with an intensity ratio of $O_{Si\text{-}def} : O_{Si} = 3.1$. The O-K-edge signals acquired from the adjacent SiO_2 regions were also compared to evaluate possible differences in the overall signal intensity. The SiO_2 region adjacent to the defective Si exhibited a higher O-K-edge signal than the SiO_2 region at the reference interface, with $O_{SiO2\text{-}def} : O_{SiO2} = 2.6$ (Fig. 2c). These results collectively suggest that FLT induces a periodic defect structure near the Si/SiO_2 interface, accompanied by a local enhancement of the oxygen signal. This periodic structure may therefore be associated with laser-induced oxygen migration or incorporation.

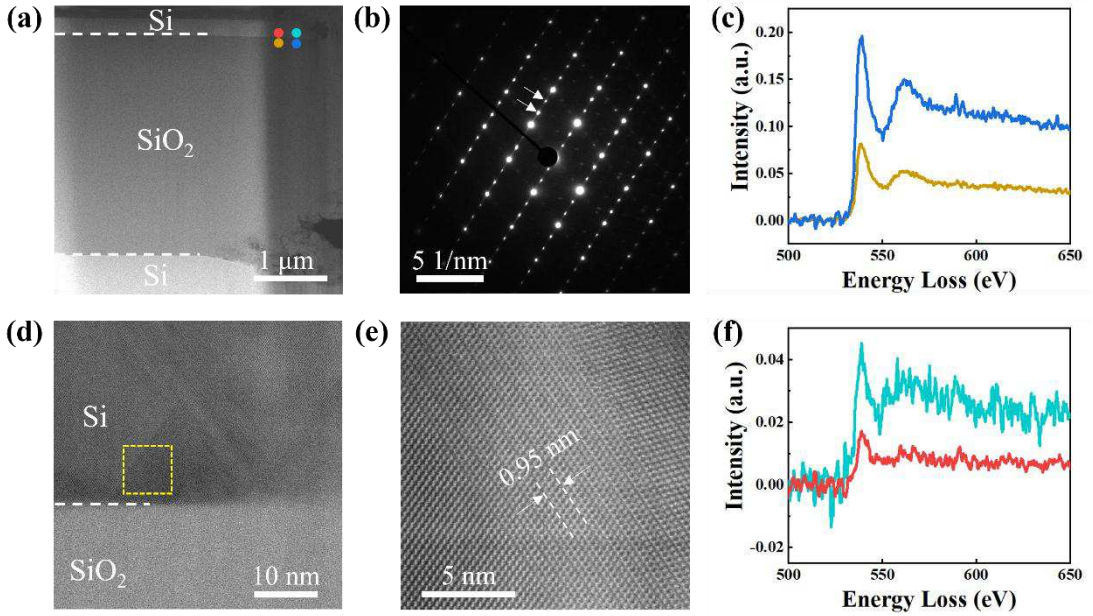

Fig. 2 | Cross-sectional microstructural and chemical characterization of the laser-treated sample. a, Cross-sectional TEM image of the laser-treated region. The white dashed lines indicate the Si/SiO_2 interfaces, and the colored markers indicate the positions from which the EELS spectra in c and f were acquired. **b,** SAED pattern acquired from crystalline Si near the Si/SiO_2 interface after laser treatment. The white arrows indicate additional weak diffraction spots. **c,** EELS spectra acquired from the SiO_2 side of interfaces with and without the laser-induced periodic defect structure. **d,** Atomic-resolution ABF-STEM image of the Si/SiO_2 interface after laser treatment. The white dashed line indicates the interface, and the yellow box marks the region enlarged in e. **e,** Atomic-resolution HAADF-STEM image of the region marked by the yellow box in d, showing a periodic lattice modulation with a repeat distance of approximately 0.95 nm. **f,** EELS spectra acquired from the Si side of interfaces with and without the laser-induced periodic defect structure.

To investigate the impact of substitutional oxygen on the electronic properties of the silicon lattice, we performed first-principles calculations on crystalline Si models with varying oxygen concentrations. As shown in Fig. 3a, the rigorous HSE06 functional calculation on DFT yields a band gap of 1.23 eV for pristine Si, which agrees well with the experimental value of approximately 1.17 eV. Upon introducing substitutional oxygen, the electronic states near the band edges undergo substantial reconstruction, resulting in a marked reduction of the band gap. Specifically, the calculated band gaps decrease to 0.80 eV and 0.53 eV for Si containing 2.08 at.% and 2.78 at.% oxygen, respectively, demonstrating a monotonic narrowing trend within this composition range. This band-gap reduction reflects the perturbation of local bonding and electrostatic environment by oxygen incorporation, which modifies both the valence- and conduction-band edge states (Fig. 3b, c). Such tunability suggests that oxygen doping offers an effective strategy for engineering narrow-

gap Si-based materials while preserving the crystalline Si host framework. These results further imply that locally oxygen-rich configurations can introduce low-energy electronic transitions absent in pristine Si, providing a plausible electronic-structure origin for the experimentally observed near-infrared emission extension. It should be noted, however, that the substitutional models employed here represent idealized defective environments rather than equilibrium oxygen configurations; in defect-free crystalline Si, oxygen typically adopts interstitial or bond-centered sites, whereas substitutional-like coordination can be stabilized in vacancy-rich regions generated by femtosecond-laser processing[29,30]. Thus, while our calculations establish a qualitative connection between oxygen incorporation and band-edge reconstruction, they do not fully delineate the complete microscopic radiative-recombination pathway. Femtosecond transient-absorption (TA) spectroscopy provides complementary experimental insight into the near-infrared optical response and excited-state dynamics of FLT-treated Si (Extended Data Fig. 5). Under 515-nm excitation, FLT-treated Si exhibits photoinduced absorption across 1200–1700 nm and a localized negative feature at approximately 1500–1550 nm, consistent with photoinduced bleaching or state filling (Extended Data Fig. 5a). The pronounced spectral evolution during the first 0.5–3.2 ps reflects rapid carrier relaxation and redistribution, whereas the persistent response from 10.3 to 97.6 ps indicates a comparatively long-lived photoexcited-state population (Extended Data Fig. 5b). Together, the calculations and TA measurements show that FLT-associated oxygen incorporation is correlated with substantial changes in the electronic structure and carrier dynamics of crystalline Si, providing a potential route to narrow-gap Si-based materials.

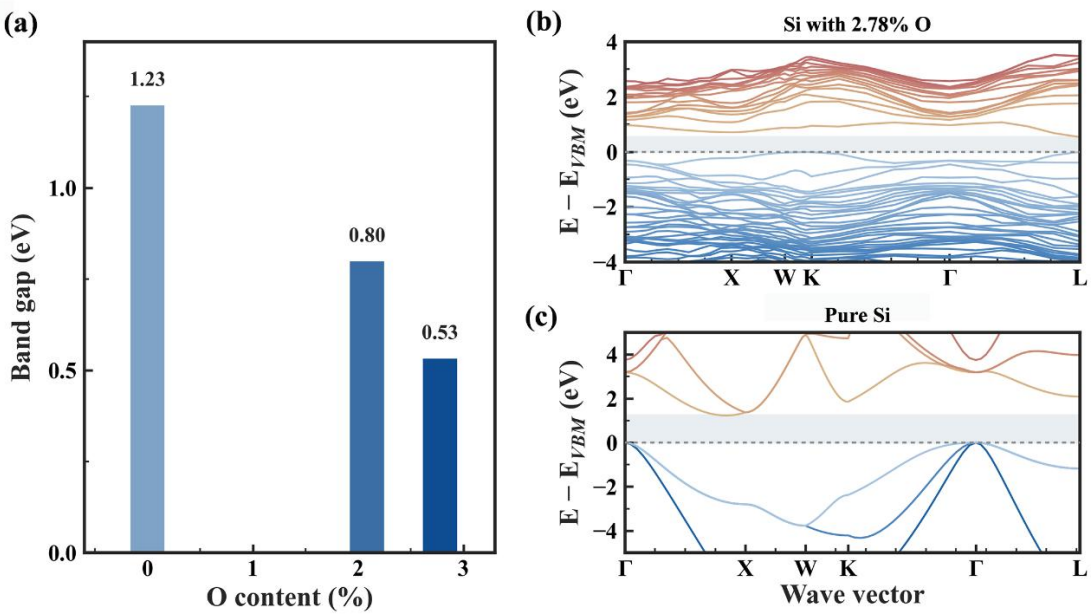

Fig. 3 | First-principles calculations. a, Silicon bandgap as a function of oxygen concentration. HSE06 band structures of **b,** pristine Si, and **c,** Si containing 2.78% nominal substitutional O.

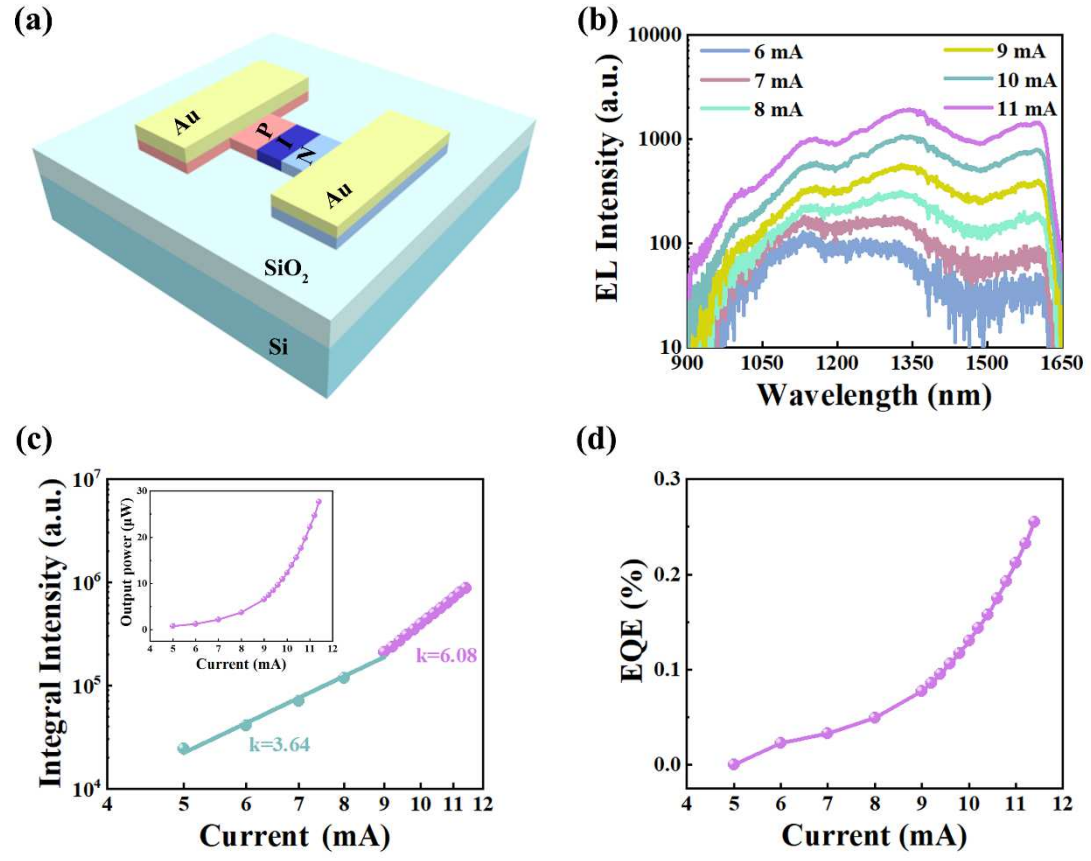

Fig. 4 | Electroluminescence of the sample. a, Schematic diagram of a broadband silicon LED. **b,** EL spectrum of infrared light at different injection currents. **c,** Relationship between infrared integral EL intensity and injection current, along with an illustration of the output power versus injection current. **d,** Relationship between EQE and injection current.

Leveraging the excellent PL properties of FLT-treated silicon, we designed a broadband LED, as shown in Fig. 4a. The manufacturing process is fully compatible with CMOS technology and involves multiple lithography and ion implantation steps to create lateral PIN junctions, which are then treated with FLT to produce a broadband electroluminescent LED (details in the Device fabrication section). Compared with untreated silicon, the FLT-treated device exhibits a substantially broader emission spectrum and enhanced emission intensity (Fig. S6). Unlike other broadband LEDs that operates through reverse avalanche breakdown[9], our LED emits light under a forward bias applied across the lateral PIN junction. Fig. 4b shows the current-dependent EL spectra of the PIN junction at room temperature, revealing ultrabroadband emission from 900 to 1650 nm, similar to that observed in the PL spectra. Additionally, Extended Data Fig.7 shows strong EL in the visible range, demonstrating that the LED exhibits broadband emission spanning 600–1650 nm. To assess whether thermal effects contribute substantially to the observed EL, we monitored the device temperature under different injection currents using infrared thermography. As shown in Extended Data Fig. 8, the maximum surface temperature after thermal stabilization was approximately 150 °C. Although infrared thermography has finite spatial resolution and does not directly measure the junction temperature of the active region, the measured surface temperature is insufficient to account for the observed EL intensity through thermal radiation within the detected spectral range. Therefore, macroscopic Joule heating alone cannot explain the measured emission. To further examine the possible contribution of thermal radiation or purely thermally activated emission, we performed an independent heating control experiment without electrical injection or optical excitation. As shown in Extended Data Fig. 9, no detectable emission similar to the EL spectrum was observed even when the device was externally heated to 300 °C, substantially above its temperature under electrical operation. Together, these measurements indicate that thermal effects are not the dominant origin of the observed EL, which is instead consistent with radiative recombination of electrically injected carriers. Fig. 4c shows the relationship between the integrated EL intensity and the injection current on a log-log scale. The slope is 3.64 at low current levels but increases to 6.08 above the threshold current of 9 mA. Notably, the super-linear dependence in both regimes, particularly the pronounced increase above 9 mA, suggests a strongly nonlinear emission process and the potential for stimulated emission. We subsequently present the EQE of infrared emission at different injection currents, as shown in Fig. 4d. The EQE increases superlinearly with the injection current over a specific current

range. At a bias current of 11.4 mA, the output power reaches 28 μW, the output power density exceeded 20 W/cm^2, and the EQE exceeds 0.26%. Notably, this EQE is calculated for emissions in the 900-1650 nm range. When the broader emission range of 600-1650 nm is considered, the total EQE is even higher. These results demonstrate that silicon, despite being an indirect bandgap semiconductor, can produce efficient ultrabroadband emission.

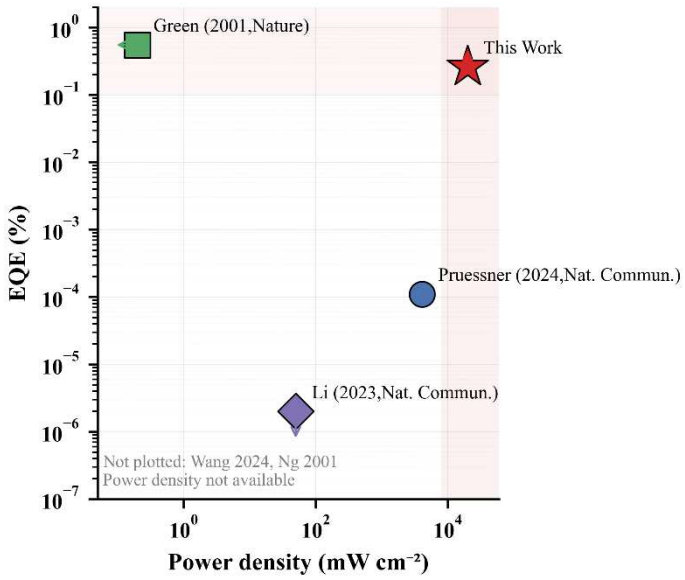

Fig. 5 | Performance comparison of the present LED with previously reported silicon-based LEDs. Both axes are plotted on logarithmic scales. References without reported power-density values are omitted.

Compared with previously reported silicon-based LEDs, our device exhibits a distinctive combination of broad spectral coverage, high EQE, and high optical power density (Fig. 5 and Table 1) [8,9,31-33]. In the EQE–power-density performance map, our device occupies the upper-right region, delivering an optical power density of approximately 2.0 × 10^4 mW/cm^2 with an EQE exceeding 0.26%. This is the highest power density and the second-highest EQE among the devices included in the comparison. Although Green et al.[32] reported a higher EQE of 0.55%, the corresponding power density was below 0.2 mW/cm^2; our device therefore achieves a more than five-orders-of-magnitude increase in power density while retaining an EQE of the same order of magnitude. Compared with the devices reported by Pruessner et al.[9] and Li et al.[8], our LED simultaneously provides substantial improvements in both EQE and power density. Moreover, its emission spans 600–1600 nm, the broadest spectral range among the devices summarized in Table 1. These results highlight that the principal advantage of our LED lies in the simultaneous realization of broadband emission, high conversion efficiency, and high optical power density rather than the optimization of

only a single performance metric.

Table 1 Comparison of the emission characteristics and optoelectronic performance of the present device with previously reported silicon-based LEDs. The reported power density of Pruessner et al. was obtained after optical focusing. n/a, not available.

Reference	Wavelength (nm)	Power (μW)	Power Density (mW/cm^2)	EQE
This Work	600-1600	>28 (11.4mA)	20000	>0.26%
Pruessner (2024)[9]	900-1600	5.1×10^{-3} (5mA)	4100 (post-focusing)	1.1×10^{-6}
Wang (2024)[31]	1500-1600	<0.1 (10mA)	n/a	8×10^{-6}
Green (2001)[32]	1050-1250	180 (40mA)	<0.2	0.55%
Ng (2001)[33]	1050-1250	19.8 (100mA)	n/a	2×10^{-4}
Li (2023)[8]	1000-1200	9.4×10^{-5} (6mA)	>50	$<2\times 10^{-8}$

Conclusion

We have demonstrated room-temperature broadband photoluminescence and forward-bias electroluminescence from femtosecond-laser-treated silicon on a standard 220-nm silicon-on-insulator platform. The treated silicon emits across approximately 600–1650 nm, with a photoluminescence external quantum efficiency of approximately 0.3% over 900–1,650 nm. A lateral PIN light-emitting diode fabricated from the treated silicon produces an optical output power of 28 μW at an injection current of 11.4 mA, corresponding to an optical power density exceeding 20 W/cm^2 and an external quantum efficiency above 0.26% over the same near-infrared range. Structural, chemical and ultrafast spectroscopic measurements indicate that femtosecond-laser treatment introduces interfacial lattice modulation and local oxygen enrichment, together with substantial changes in the electronic structure and carrier dynamics of silicon. These observations support an association between the laser-induced modifications and the enhanced broadband emission. The combination of broad spectral coverage, high optical power density and electrical operation on a standard SOI platform makes this approach promising for integrated spectroscopy, sensing and imaging.

References

1 Wang, Z. *et al.* Novel light source integration approaches for silicon photonics. *Laser Photonics Rev.* **11**, 1700063(2017).

2 Priolo, F., Gregorkiewicz, T., Galli, M. & Krauss, T. F. Silicon nanostructures for photonics and photovoltaics. *Nature Nanotechnology* **9**, 19-32(2014).

3 De Koninck, Y. *et al.* GaAs nano-ridge laser diodes fully fabricated in a 300-

mm CMOS pilot line. *Nature* **637**, 63-69(2025).
4 Komljenovic, T. *et al.* Photonic integrated circuits using heterogeneous integration on silicon. *Proceedings of the IEEE* **106**, 2246-2257(2018).
5 Shang, C. *et al.* High-temperature reliable quantum-dot lasers on Si with misfit and threading dislocation filters. *Optica* **8**, 749-754(2021).
6 Liu, Y. *et al.* A photonic integrated circuit–based erbium-doped amplifier. *Science* **376**, 1309-1313(2022).
7 Liao, K. *et al.* Hetero-integrated perovskite/Si_3N_4 on-chip photonic system. *Nat. Photonics* **19**, 358-368(2025).
8 Li, Z. *et al.* A sub-wavelength Si LED integrated in a CMOS platform. *Nat. Commun.* **14**, 882(2023).
9 Pruessner, M. W. *et al.* Broadband near-infrared emission in silicon waveguides. *Nat. Commun.* **15**, 4639(2024).
10 de Cea, M., Li, Z., Notaros, M., Notaros, J. & Ram, R. J. Single-mode waveguide-coupled light emitting diodes in unmodified silicon photonics fabrication processes. *APL Photonics* **8**, 081301(2023).
11 Hirschman, K., Tsybeskov, L., Duttagupta, S. & Fauchet, P. Silicon-based visible light-emitting devices integrated into microelectronic circuits. *Nature* **384**, 338-341(1996).
12 Chynoweth, A. & McKay, K. Photon emission from avalanche breakdown in silicon. *Physical Review* **102**, 369(1956).
13 Ma, F. *et al.* Highly Bright Silicon Nanocrystal White Light-Emitting Diodes With Luminance in Excess of 10000 cd m^{-2}. *Laser Photonics Rev.* **19**, 2402164(2025).
14 Ryckeboer, E., Bockstaele, R., Vanslembrouck, M. & Baets, R. Glucose sensing by waveguide-based absorption spectroscopy on a silicon chip. *Biomedical optics express* **5**, 1636-1648(2014).
15 Stievater, T. H. *et al.* Trace gas absorption spectroscopy using functionalized microring resonators. *Optics letters* **39**, 969-972(2014).
16 Li, A. & Fainman, Y. Integrated Silicon Fourier Transform Spectrometer with Broad Bandwidth and Ultra-High Resolution. *Laser Photonics Rev.* **15**, 2000358(2021).
17 Singh, N. *et al.* Octave-spanning coherent supercontinuum generation in silicon on insulator from 1.06 μm to beyond 2.4 μm. *Light Sci. Appl.* **7**, 17131-17131(2018).
18 Zia, H., Ye, K., Klaver, Y., Marpaung, D. & Boller, K.-J. Ultraefficient on-chip supercontinuum generation from sign-alternating-dispersion waveguides. *Advanced photonics research* **4**, 2200296(2023).
19 Singh, N. *et al.* Octave-spanning coherent supercontinuum generation in silicon on insulator from 1.06 μm to beyond 2.4 μm. *Light Sci. Appl.* **7**, 17131-17131(2017).
20 Shi, Z. *et al.* Bright compact ultrabroadband source by orthogonal laser-sustained plasma. *Light Sci. Appl.* **13**, 274(2024).
21 Tyndall, N. F. *et al.* Figure-of-Merit Characterization of Hydrogen-Bond Acidic

Sorbents for Waveguide-Enhanced Raman Spectroscopy. *ACS Sensors* **5**, 831-836(2020).

22 Ji, X. *et al.* Millimeter-scale chip–based supercontinuum generation for optical coherence tomography. *Sci. Adv.* **7**, eabg8869(2021).

23 Zhang, C. *et al.* Lighting up silicon nanoparticles with Mie resonances. *Nat. Commun.* **9**, 2964(2018).

24 Panmai, M. *et al.* Highly efficient nonlinear optical emission from a subwavelength crystalline silicon cuboid mediated by supercavity mode. *Nat. Commun.* **13**, 2749(2022).

25 Yan, Z. *et al.* A monolithic InP/SOI platform for integrated photonics. *Light Sci. Appl.* **10**, 200(2021).

26 Fadaly, E. M. T. *et al.* Direct-bandgap emission from hexagonal Ge and SiGe alloys. *Nature* **580**, 205-209(2020).

27 Yoo, Y.-S., Roh, T.-M., Na, J.-H., Son, S. J. & Cho, Y.-H. Simple analysis method for determining internal quantum efficiency and relative recombination ratios in light emitting diodes. *Appl. Phys. Lett.* **102**, 211107(2013).

28 Jeong, S.-H. *et al.* Characterizing the Efficiency of Perovskite Solar Cells and Light-Emitting Diodes. *Joule* **4**, 1206-1235(2020).

29 Artacho, E. *et al.* Interstitial oxygen in germanium and silicon. *Physical Review B* **56**, 3820(1997).

30 Capron, N., Maji, R., Luppi, E. & Contreras-García, J. The role of Si vacancies in the segregation of O, C, and N at silicon grain boundaries: An ab initio study. *The Journal of Chemical Physics* **155**, 174704(2021).

31 Wang, X. *et al.* Analytical impact-excitation theory of Er/O/B codoped Si light-emitting diodes. *Physical Review Letters* **132**, 246901(2024).

32 Green, M. A., Zhao, J. H., Wang, A. H., Reece, P. J. & Gal, M. Efficient silicon light-emitting diodes. *Nature* **412**, 805-808(2001).

33 Ng, W. L. *et al.* An efficient room-temperature silicon-based light-emitting diode. *Nature* **414**, 470-470(2001).

34 Shin, J. C. *et al.* Electrically Confined Electroluminescence of Neutral Excitons in WSe_2 Light-Emitting Transistors. *Adv. Mater.* **36**, 2470106(2024).

35 Kwon, J. *et al.* Multioperation-Mode Light-Emitting Field-Effect Transistors Based on van der Waals Heterostructure. *Adv. Mater.* **32**, 2003567(2020).

36 Higashitarumizu, N., Tajima, S., Kim, J., Cai, M. & Javey, A. Long operating lifetime mid-infrared LEDs based on black phosphorus. *Nat. Commun.* **14**, 4845(2023).

Methods

FLT

we use the FemtoLAB system from UAB Altechna R&D for femtosecond laser treating. The system features a Pharos femtosecond laser with a central wavelength of 515 nm, a pulse width of 290 fs, and repetition rate of 100 kHz, allowing precise control of laser energy through attenuation filters. The laser beam is focused onto the sample surface with a 10× objective lens (NA=0.26), delivering 300 nJ of energy for the treating process.

First-principles calculations

First-principles calculations were performed using the plane-wave pseudopotential method implemented in the Quantum ESPRESSO package. The exchange–correlation energy was initially treated within the generalized-gradient approximation using the Perdew–Burke–Ernzerhof (PBE) functional. Norm-conserving pseudopotentials were employed to describe the interactions between the valence electrons and ionic cores of Si and O. The kinetic-energy cutoff for the plane-wave basis set was set to 80 Ry. Oxygen-incorporated Si models were constructed by replacing one Si atom in each crystalline Si supercell with one O atom. The resulting O concentrations were 2.08, 2.78, 4.17, and 8.33 at.%, where the concentration was defined as the atomic fraction of O in the corresponding supercell. For each model, both the atomic positions and lattice parameters were fully relaxed until the prescribed convergence criteria for the total energy, atomic forces, and residual stress were satisfied. The relaxed structures were subsequently used for electronic-structure calculations. Because semilocal PBE calculations generally underestimate the band gap of Si, the electronic structures and band gaps were further calculated using the screened hybrid Heyd–Scuseria–Ernzerhof functional (HSE06). The exact-exchange q-point mesh was explicitly tested, and an nqx1 = nqx2 = nqx3 = 2 mesh was used for the doped supercell calculations unless otherwise stated. For pristine Si, a primitive-cell HSE06 reference calculation with a denser 8×8×8 k-point mesh and nqx = 4. The resulting HSE06 band gap of pristine Si was 1.23 eV, close to the experimental value of approximately 1.17 eV, confirming that the adopted hybrid-functional settings provide a reasonable description of the electronic structure of crystalline Si.

Device fabrication

The LEDs are fabricated on a standard 220 nm SOI substrate using a p-type <100> monocrystalline silicon wafer (single-side polished wafers, with a resistivity of about 10 Ω·cm, and a roughness of less than 0.5 nm). First, ultraviolet lithography combined with silicon dry etching is employed for patterning the devices, which facilitates device isolation and mitigates leakage currents. Next, ultraviolet lithography is used for further patterning, coupled with ion implantation to form the PN junction. The specific parameters are as follows: the boron ion implantation energy is 20 keV with a dose of 9×10^{14} cm^{-2}, while the phosphorus ion implantation energy is 60 keV, also with a dose of 9×10^{14} cm^{-2}. Upon completion of ion implantation, the devices undergo a rapid thermal annealing process at 950°C for 30 seconds to activate the implanted dopant ions. After the annealing, standard lift-off processing is used to fabricate the electrodes, which consist of a 10 nm chromium layer and a 50 nm gold layer, where the chromium layer serves as an adhesion layer, and the gold layer functions as the conductive layer. Finally, FLT is performed on the intrinsic region (I region) of the devices.

Photoluminescence Testing

Fluorescence signals are collected using the WITec confocal Raman system Alpha300R. The visible light

diffraction grating is 300 g/mm (BLZ 750 nm), while the infrared grating is 150 g/mm (BLZ 1250 nm). The system has an excitation wavelength of 532 nm and employs a 10× objective lens (NA=0.25). The power of the pump laser is adjusted using an attenuation filter and measured with a calibrated photodiode (Thorlabs). Extended Data Fig.1 depicts the PL spectra of the silicon pre- and post-femtosecond FLT. It is evident from the comparison that the post-treatment PL spectrum manifests a prominent broadening effect with an expanded wavelength range, accompanied by a multi-order-of-magnitude elevation in luminous intensity and marked optimization of optical radiation performance—thereby providing direct evidence for the effective modulation of silicon's luminescent behavior by femtosecond laser. Extended Data Fig. 2 illustrates the visible light emission spectrum of the sample subsequent to FLT. Notably, the visible spectrum exhibits a distinct broadband profile, and its spectral evolution trend is consistent with that of the near-infrared (NIR) spectrum (as reported in the Fig. 1). This congruence in spectral response between the visible and NIR regions underscores the universality of FLT-induced modulation on the sample's luminescent behavior, demonstrating that the laser treatment enables uniform regulation of the emission characteristics across multiple wavelength regimes.

Electroluminescence Testing

EL signals were also acquired using a WITec Alpha300R confocal Raman system, which was configured with a 300 g/mm visible light diffraction grating (BLZ = 750 nm), a 150 g/mm infrared diffraction grating (BLZ = 1250 nm), and a 10× objective lens (NA = 0.25). Extended Data Fig.3 presents the EL spectra of the same LED under an injection current of 10 mA, recorded before and after FLT. Notably, the LED treated by FLT exhibits a distinct broadening of the EL spectrum and a significant enhancement in luminous intensity compared to the pristine device, which confirms the unique role of fs laser in optimizing the luminous performance of the device. Extended Data Fig. 4 shows the visible-light EL spectrum of the LED after FLT, featuring broadband emission. Importantly, the variation trend of EL intensity with injection current is consistent with that of the near-infrared spectrum presented in Fig. 3.

Transient Absorption Spectroscopy Testing

Microregion testing is conducted using the TA100-1030NM-NIR-MIC ultrafast transient absorption spectroscopy system from the time tech spectra, which features a maximum time window of 8 ns. The primary pump light (515 nm, 100 kHz) excites carriers from the ground state to an excited state. A weaker, time-delay-tunable white light (1200-1700 nm) is then used for detection at the location where the pump light overlaps with the sample surface.

Extraction of EQE

We used the WITec Alpha300R system to measure the photoluminescent and electroluminescent EQE of silicon samples treated with FLT. In this process, accurately calibrating the total loss caused by all components in the optical path is crucial for ensuring the reliability of the test results. Typically, we estimate the total loss by assuming the optical path conditions and accumulating the known loss coefficients of each component. However, due to significant differences in optical path design, component parameters, and environmental conditions across different experiments, this method often leads to substantial deviations between the estimated values and the actual situation. To overcome this challenge and simplify the measurement process, we adopte a method based on the intensity ratio of a traditional LED to the sample's photoluminescence (PL) [28,34-36]. Specifically, we select the Hamamatsu LED (L12509-0155G) as the reference standard for the system's total loss. During the measurement, to ensure accuracy and comparability, we incorporate an appropriate infrared attenuator into the Alpha300R system to attenuate the fluorescent signal from the standard Hamamatsu LED to a level comparable to that of the infrared fluorescent signal from the sample under test. Subsequently, by precisely measuring

and comparing the PL/EL spectral areas of the standard LED and the sample, we can accurately calculate the optical power of the sample using the mathematical relationships between them. Once we obtain the optical power data, we combine it with relevant parameters such as the pump light power and, based on the definition and calculation formula of EQE, accurately determine the photoluminescent and electroluminescent EQE of the sample under test.

$$EQE = \frac{P_{out}}{P_{in}}$$

Data availability: All data are available in the main text or the supplementary materials.

Acknowledgment

We acknowledge Photon Technology (Zhejiang) Co., Ltd. (PHOTEC) for technical support and access to the Qumi-2000 single photon microscope, which was used to acquire the fluorescence lifetime data presented in this work. This work was supported by National Natural Science Foundation of China (62575294, 62305354, 52476080, 62574081) and Shanghai Science and Technology Commission Foundation (24TS1400400).

Author contributions: Jiajing He conceived the idea and supervised the project. Jiajing He and Xiaobo Li designed the experiments. Xiaobo Li prepared the samples and performed measurements. Xinyu Zhang performed the simulations. Xiaomei Li conducted the TEM characterization. Xiaobo Li, Jiajing He, Yaping Dan, Xin Wu, Hua Bao, Jun Wang, Xinyu Zhang analyzed the data and discussed the results. Xiaobo Li and Jiajing He wrote the manuscript with input from all authors.

Competing interests: Authors declare that they have no competing interests.

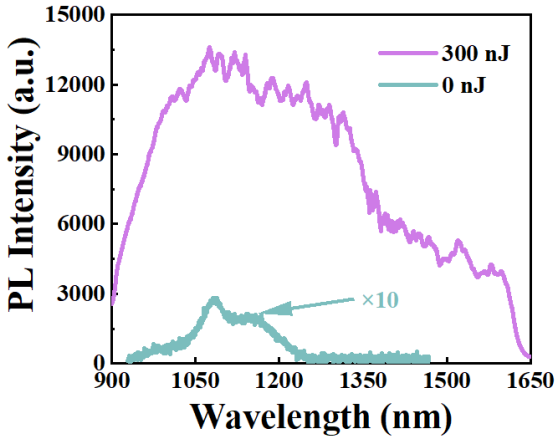

Extended Data Fig.1 | Comparison of PL intensity between pure silicon and FLT silicon.

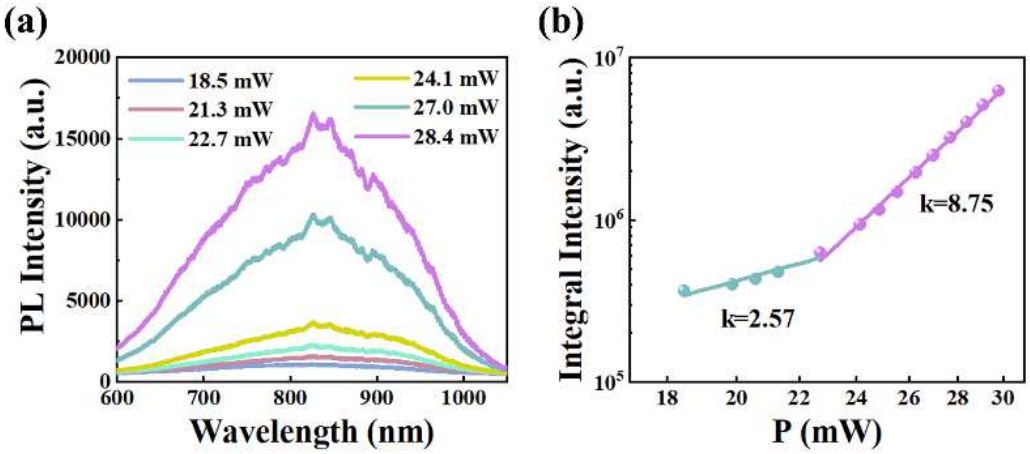

Extended Data Fig.2 | Visible light PL characterization of the samples. a, Photoluminescence spectra of visible light excited by varying powers. **b,** Relationship between photoluminescence integral intensity of visible light and pump power, with the straight line representing the linear fit of photoluminescence integral intensity with variable pump power (log-log scale).

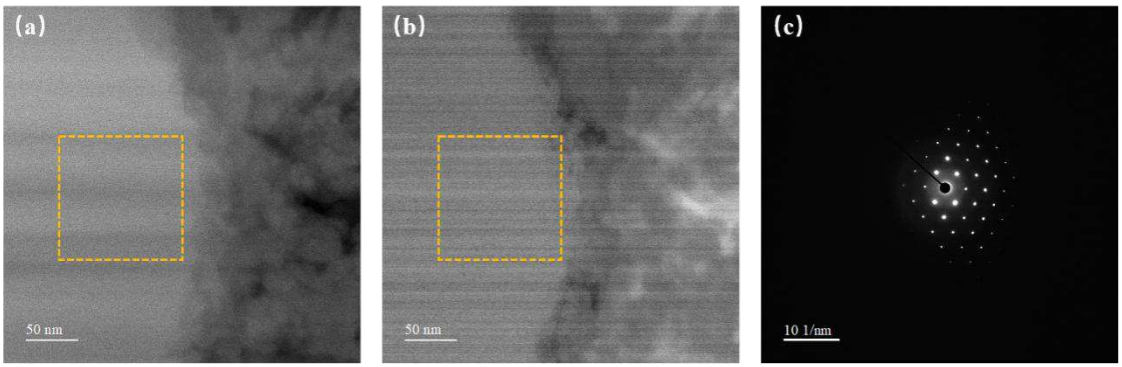

Extended Data Fig.3 | Microstructure of the laser-treated control sample prepared without oxygen treatment. a, HAADF-STEM image of the transition region between crystalline and amorphous Si in the control sample. The yellow dashed box indicates the region selected for electron diffraction. **b,** Corresponding ABF-STEM image showing a direct boundary between crystalline and

amorphous Si, without a discernible intermediate periodic defect structure. **c,** SAED pattern acquired from the region indicated by the yellow dashed box. The pattern primarily contains the fundamental reflections of crystalline Si and diffuse scattering associated with the amorphous structure, without the additional weak diffraction spots observed in the oxygen-treated sample.

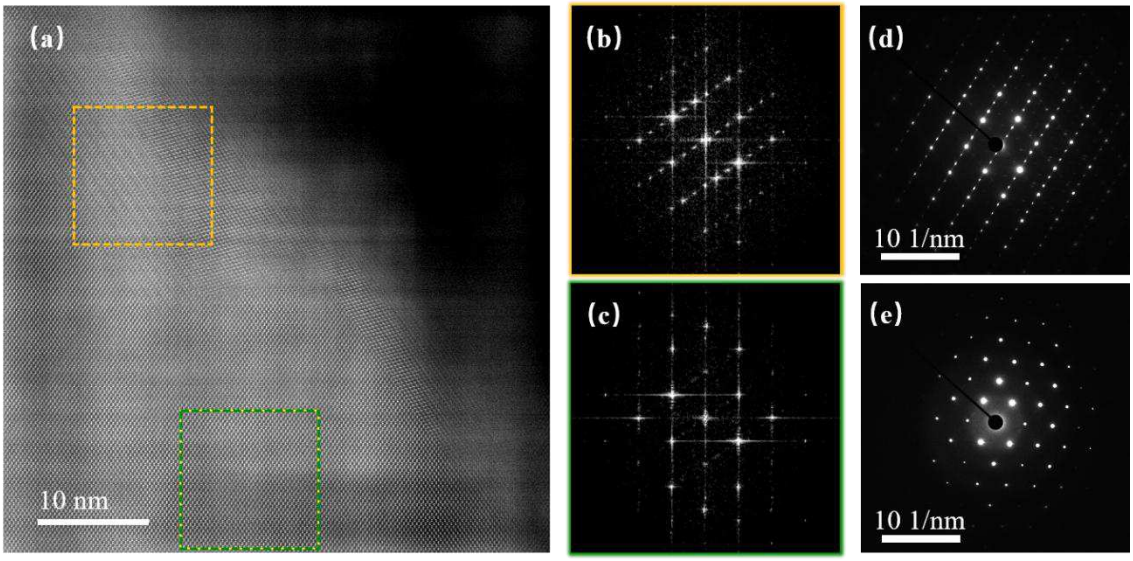

Extended Data Fig.4 | Comparison of the local FFT and SAED patterns from the periodic defect and reference crystalline Si regions. a, Atomic-resolution STEM image containing the periodic defect and reference crystalline Si regions. The yellow and green boxes mark the periodic defect and reference crystalline Si regions, respectively. **b,** Local FFT pattern of the periodic defect region marked by the yellow box in a, showing additional weak reflections besides the fundamental Si lattice reflections. **c,** Local FFT pattern of the reference crystalline Si region marked by the green box in a, predominantly showing the fundamental reflections of the Si lattice. **d,** SAED pattern acquired from the periodic defect region, showing additional diffraction spots. **e,** SAED pattern acquired from the reference crystalline Si region, without the corresponding additional reflections.

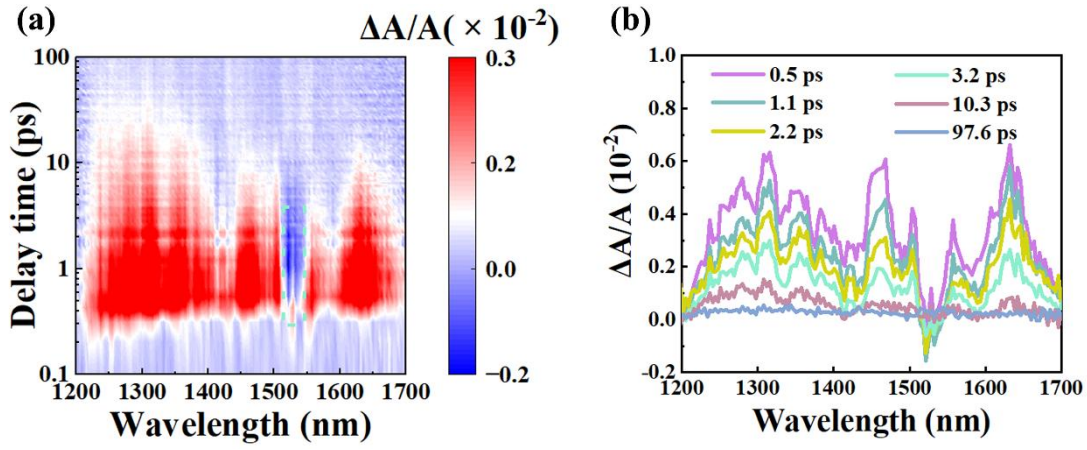

Extended Data Fig. 5 | Ultrafast carrier dynamics in FLT-treated silicon probed by femtosecond TA spectroscopy. a, Two-dimensional TA map recorded at room temperature under 515 nm excitation with a probe wavelength range of 1200–1700 nm. The differential absorption signal (ΔA/A) exhibits broad positive photoinduced-absorption features throughout the near-infrared region and a localized negative feature at approximately 1,500–1,550 nm (dashed box). The negative signal may be related to the excitation of electrons by the Pauli blocking. **b,**

Representative TA spectra extracted at pump–probe delays of 0.5, 1.1, 2.2, 3.2, 10.3, and 97.6 ps. Substantial changes in the spectral amplitude and profile occur during the first 0.5-3.2 ps, indicating rapid early-time carrier relaxation and redistribution. The slower evolution and residual signal observed from 10.3 to 97.6 ps suggest the excited state stabilizes in FLT-treated silicon.

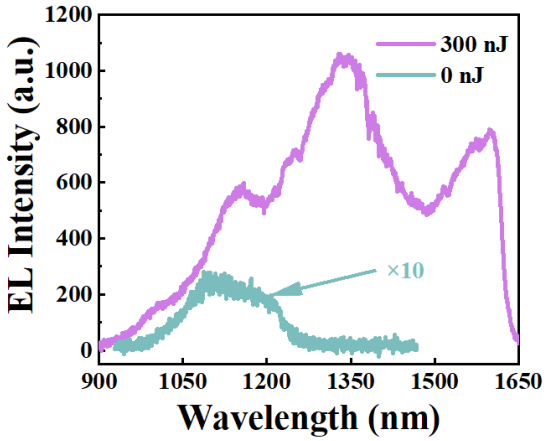

Extended Data Fig.6 | Comparison of EL intensity between pure silicon LEDs and FLT LEDs with identical structures.

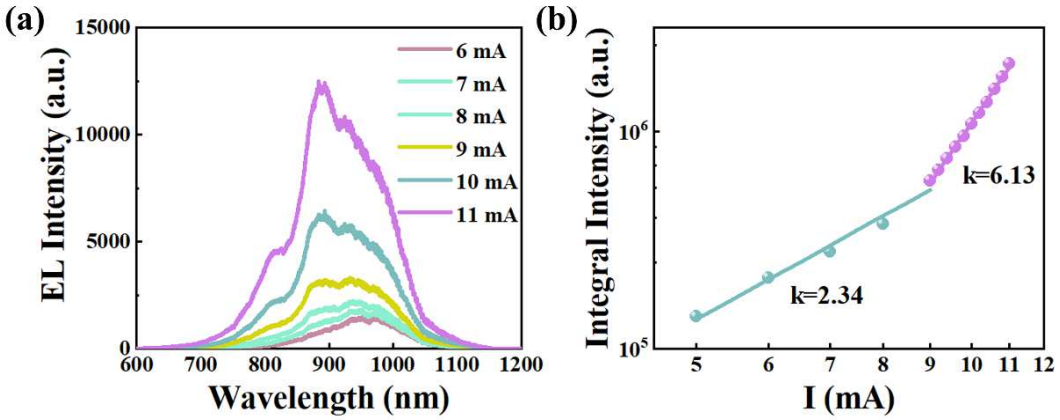

Extended Data Fig.7 | Visible light EL characterization of the LED. a, Visible light EL spectrum under different injection currents. **b,** Relationship between the integral EL intensity of visible light and the injection current (log-log scale).

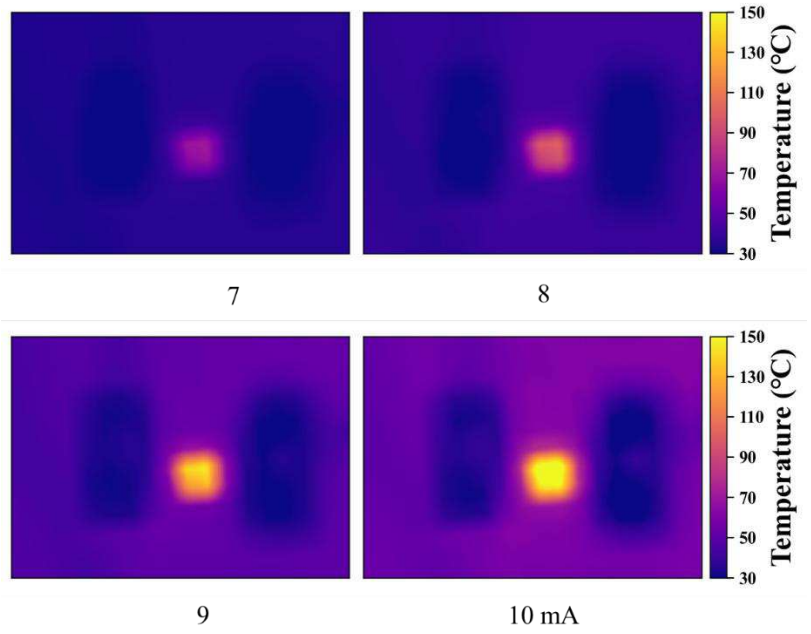

Extended Data Fig.8 | Measuring the temperature of broadband LEDs at different currents using an infrared camera.

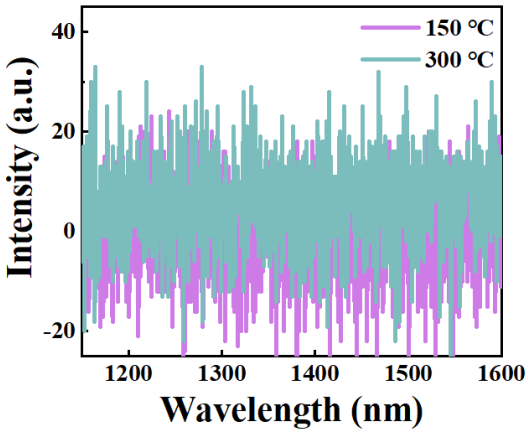

Extended Data Fig.9 | PL of the Silicon at different temperatures After FLT. Emission spectra recorded from the FLT-treated silicon sample under external heating to 150 °C and 300 °C, without electrical injection or optical excitation. No detectable emission corresponding to the electrically driven EL spectrum is observed, even at 300 °C, a temperature substantially higher than that measured during device operation.